iScience

CellPress
OPEN ACCESS

Article

Donor-acceptor-type poly[chalcogenoviologen-*alt*-triphenylamine] for synaptic biomimicking and neuromorphic computing

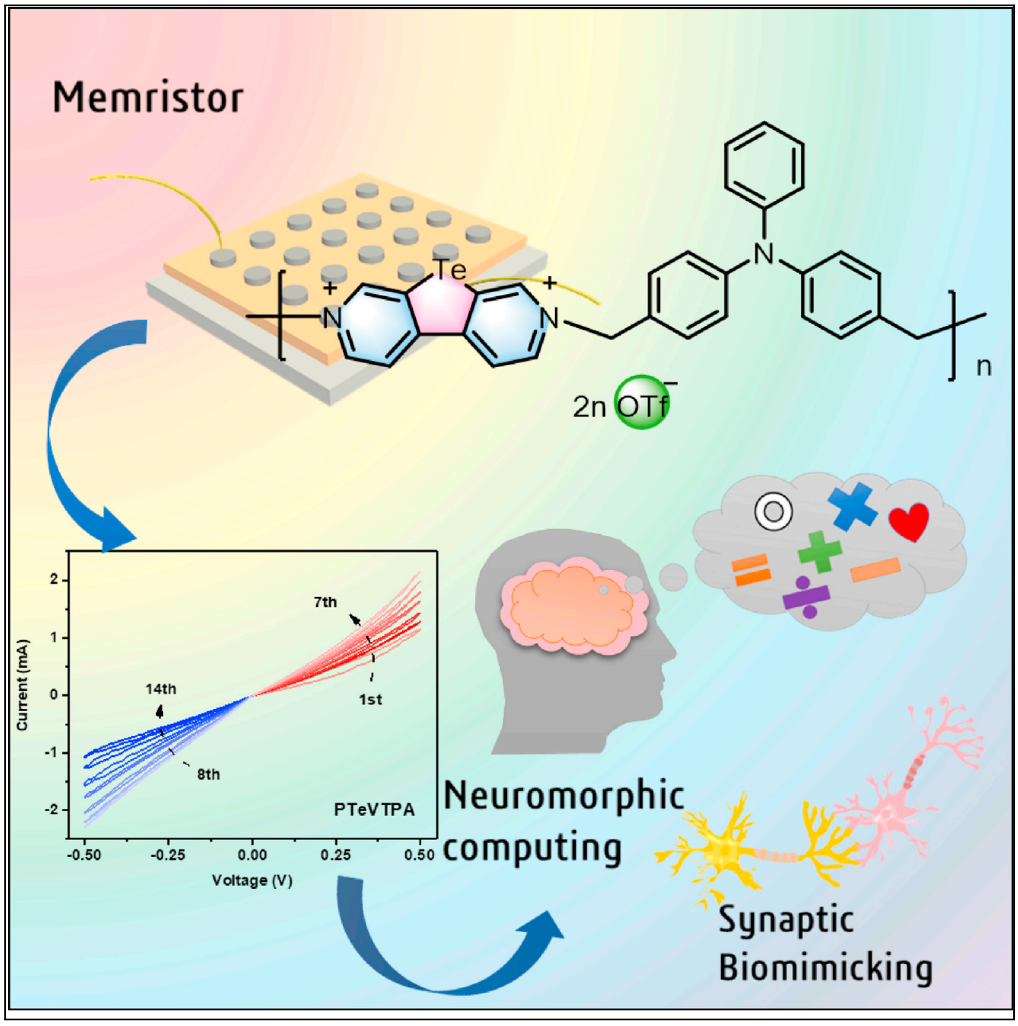

Zhizheng Zhao, Qiang Che, Kexin Wang, ..., Yubin Fu, Bin Zhang, Yu Chen

chentangyu@yahoo.com (Y.C.)
amzhangbin@126.com (B.Z.)
yubin.fu@tu-dresden.de (Y.F.)

Highlights

Poly[chalcogenoviologen-*alt*-triphenylamine] (PCVTPA) has been synthesized

PCVTPA-based memristor exhibits excellent memristive performance

PCVTPA-based memristor is capable of executing arithmetic operations on decimal

PCVTPA shows great potential in constructing intelligent computing system

Zhao et al., iScience *25*, 103640
January 21, 2022
https://doi.org/10.1016/j.isci.2021.103640

iScience

CellPress
OPEN ACCESS

Article

Donor-acceptor-type poly[chalcogenoviologen-*alt*-triphenylamine] for synaptic biomimicking and neuromorphic computing

Zhizheng Zhao,[1] Qiang Che,[1] Kexin Wang,[1] Mohamed E. El-Khouly,[2] Jiaxuan Liu,[1] Yubin Fu,[3,*] Bin Zhang,[1,*] and Yu Chen[1,4,*]

SUMMARY

Polymer memristors are preeminent candidates for low-power edge computing paradigms. Poly[chalcogenoviologen-*alt*-triphenylamine] (PCVTPA) has been synthesized by direct coupling of chalcogeno-viologen as electron acceptor and 4-(bromomethyl)-N-(4-(bromo-methyl)phenyl)-N-phenylaniline as electron donor. The introduction of chalcogen atoms (S, Se, Te) into viologen scaffolds can greatly improve electrical conductive, electrochemical, and electrochromic properties of the materials when compared with the conventional viologens. Taking PTeVTPA as an example, the as-fabricated electronic device with a configuration of Al/PTeVTPA/ITO exhibits excellent multilevel storage and history-dependent memristive switching performance. Associated with the unique memristive behavior, the PTeVTPA-based device can not only be used to emulate the synaptic potentiation/depression, the human's learning and memorizing functions, and the transition from short-term synaptic plasticity to long-term plasticity but also carry out decimal arithmetic operations as well. This work will be expected to offer a train of new thought for constructing high-performance synaptic biomimicking and neuromorphic computing system in the near future.

INTRODUCTION

The human memory mainly benefits from the natural evolution of neural networks that exhibit several outstanding properties such as massive parallel processing, in-memory computing architecture, event-driven operation and others. Since the discovery of the first real memristor at HP Labs in 2008 (Strukov et al., 2008), great efforts have been devoted to developing novel memristive functional materials and devices to construct artificial neural networks for neuromorphic computation and emulate the physiological functions (e.g., the learning, memorizing, forgetting, decision-making, and judging actions) of biological synapses (Chen et al., 2014; Zhang et al.,2018, Zhang et al., 2019, 2020, Zhang et al., 2021; Van De Burgt et al., 2018; Choi et al.,2018, 2020; Liu et al.,2016, 2018; Li et al., 2017; Wan et al., 2020; Kim et al., 2018; Wang et al., 2014, 2015; Ren et al., 2020; McFarlane et al., 2020). Recently, it was found that the negative photoconductance effect observed impressively in the high resistance state branch of the resistive switching memory enabled the memristor function to be extended to both memory logic display and multistate data storage (Zhou et al., 2021). The combination of multiple physical properties (memristive and capacitive) in a single device could also prefigure potential multifunctional applications (Sun et al., 2020). The memristor-based brain-like intelligent computing system not only can improve significantly the computing capability of modern computer systems via massive parallelism at very low power consumption but also can overcome the von Neumann bottleneck (i.e., the limited throughput between the memory and central processing unit) when dealing with data-intensive tasks.

A large number of inorganic materials are used to construct the memristor devices and still play a dominant role in fabricating memristors with superior processing efficiency and enormous storage capacity so far (Choi et al., 2018; Li et al., 2017; Wan et al., 2020; Kim et al., 2018). In comparison with the inorganic and organic small molecule counterparts, polymer materials show higher intrinsic flexibility and ease for solution processing. The solution processing capability allows them to be handled *via* low-cost techniques of dip coating, blade casting, spray coating, spin coating, roller-coating, and even ink-jet printing, making the

[1]Key Laboratory for Advanced Materials and Joint International Research Laboratory of Precision Chemistry and Molecular Engineering, Feringa Nobel Prize Scientist Joint Research Center, School of Chemistry and Molecular Engineering, East China University of Science and Technology, Shanghai 200237, China

[2]Institute of Basic and Applied Sciences, Egypt-Japan University of Science and Technology (E-JUST), Alexandria 21934, Egypt

[3]Center for Advancing Electronics Dresden (cfaed) & Department of Chemistry and Food Chemistry, Technische Universität Dresden, Dresden 01062, Germany

[4]Lead contact

*Correspondence: chentangyu@yahoo.com (Y.C.), amzhangbin@126.com (B.Z.), yubin.fu@tu-dresden.de (Y.F.)

https://doi.org/10.1016/j.isci.2021.103640

fabrication procedure of electronic and optoelectronic devices potentially more economical without the involvement of vacuum deposition procedure (Chen et al., 2014; Liu et al., 2018; Ling et al., 2008; Lin et al., 2014; Liu and Chen, 2011). Since 2005, polymer memories have been proposed to revolutionize electrical applications by providing extremely inexpensive, lightweight, and transparent modules that can be fabricated onto plastic, glass, or the top layer of the complementary metal-oxide semiconductor circuits. Similar to these inorganic materials, some polymer functional materials, including metal-containing polymers, polymer-based multi-component redox systems, and pure polymers, have also been found to exhibit excellent memristive performance in recent years (Chen et al., 2014; Zhang et al.,2018, Zhang et al., 2019, 2020, Zhang et al., 2021; Wang et al.,2014, 2015; Liu et al., 2016; Ren et al., 2020; McFarlane et al., 2020; Pincella et al., 2011; Bandyopadhyay et al., 2011). With these polymer memristors, one can observe nonlinear transmission characteristics similar to that of a biological synapse. More importantly, their memristive performance can be easily tuned through innovative molecular design cum synthesis strategy.

Polymer memristors are preeminent candidates for low-power edge computing paradigms. In our pioneering works, we reported a proof-of-concept polymer memristive processing-memory unit that demonstrates programmable information storage and processing capabilities (Zhang et al., 2019). By using polyfluorene functionalized with triphenylamine and ferrocene moieties side chains as an active layer, the as-fabricated electronic device, which shows excellent memristive switching and multilevel memory performance, is capable of executing multilevel memory; decimal arithmetic operations of addition, subtraction, multiplication, and division; as well as simple Boolean logic operations. Recently, we designed and synthesized a two-dimensional conjugated polymer PBDTT-BQTPA (Zhang et al., 2021). This material-based electronic device exhibited a rapid transition from the OFF state to the ON state within ~32 ns. More importantly, we successfully achieved a record high 90% production yield of polymer memristors with low power and miniaturization potentials. The reliability of the as-fabricated memristor was greatly enhanced by the delocalized resistive switching, making downscaling of the device to 100-nm scale possible for low-power edge computing applications. We also observed for the first time the self-rectified memristive effect in a metal-free soluble organic oligomer PFD-8CN (Wang et al., 2015).

It would be quite desirable to integrate programmable multilevel storage, synaptic biomimicking, and neuromorphic computing in the same electronic device. As one of the most promising candidates for energy, electrochromism, gas separation and storage, and electronic and optoelectronic applications, viologens (Vs) composed of conjugated bi-/multipyridyl groups show a number of unique properties such as reversible redox behavior, ionic and localized conjugation, bio-sensitive response, and electrochromic and radical-rich features (Mi et al., 2019; Kortz et al., 2019; Ding et al., 2019; Zhang et al., 2017; Yang et al., 2021; Sluysmans et al., 2020; Lipke et al., 2017; Li et al.,2018, 2019). For reduction of Vs, all of their three reductive states (neutral, radical cation, and dication) are thermodynamically stable. Also, Vs can be used as a strong electron-withdrawing unit to construct donor-acceptor-type organic/polymeric functional materials. On the other hand, triphenylamine (TPA) and its derivatives have been widely applied in the fields of optoelectronics and electronics owing to their 3D steric profile, low ionization potentials, inner redox activity, and excellent UV light-harvesting ability (Fang and Yamamoto, 2004; Zhang et al., 2018; El-Khouly et al., 2009; Ego et al., 2002). Based on these backgrounds, in this work, we designed and synthesized a novel conjugated donor-acceptor polymer, poly[chalcogenoviologen-*alt*-triphenylamine] (PCVTPA, including PSVTPA, PSeVTPA, and PTeVTPA), by direct coupling of 4-(bromomethyl)-N-(4- (bromomethyl)phenyl)-N-phenylaniline as electron donor and chalcogenoviologen as electron acceptor, as shown in Scheme 1. The introduction of chalcogen atoms (S, Se, Te) into viologen scaffolds can greatly improve electrochemical, electrical conductive, and electrochromic properties of the materials (Lipke et al., 2017; Li et al., 2019). Like Vs, poly (chalcogenoviologen) (PCV) also exhibits good electron-withdrawing characteristics (Lipke et al., 2017; Li et al., 2019; Stolar et al., 2016). As a result, the as-prepared Al/PCVTPA/ITO sandwich structure device exhibited excellent history-dependent memristive switching performance. With this device one can not only easily realize the biological stimuli of the "learning→ forgetting→ re-learning→re-forgetting" processes associated to the human's learning/memory functions but also execute decimal arithmetic operations of addition, subtraction, multiplication, and division. These results demonstrate that this material shows the great potential in constructing artificial neural networks for neuromorphic computation. As comparison, we also synthesized poly[4,4-bipyridine-*alt*-triphenylamine] (PBPTPA) under the same experimental conditions. Unlike PCVTPA, PBPTPA did not show any apparent memristive effect.

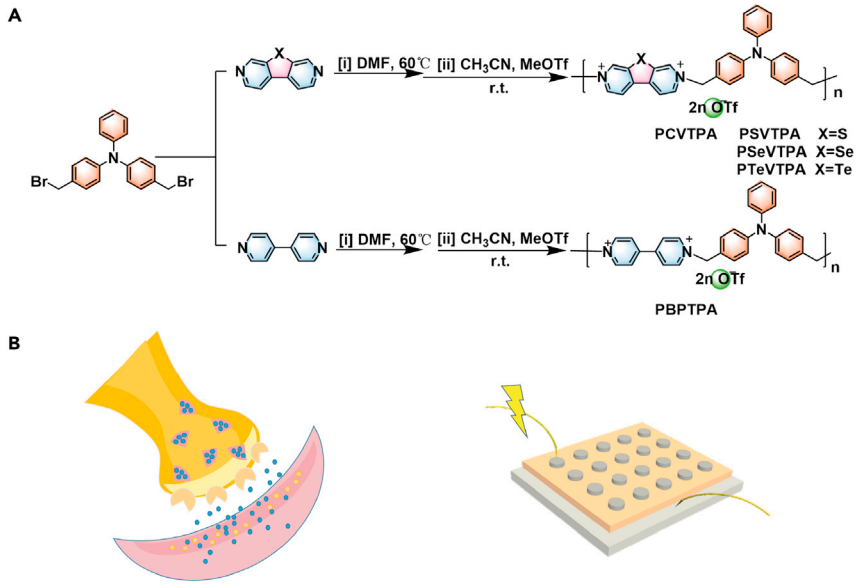

Scheme 1. Synthesis route and Schematic illustration

(A) Synthesis of PCVTPA (PSVTPA, PSeVTPA, PTeVTPA) and PBPTPA.

(B) Schematic illustration of the Al/polymer/ITO memristor and the biological synapse.

RESULTS AND DISCUSSION

Both the PCVTPA and PBPTPA polymers are highly soluble in acetonitrile and *N*, *N*-dimethylformamide (DMF). Their weight-average molecular weights/polydispersity indexes, which were determined with a gel permeation chromatograph PL-GPC50 using polystyrene standards eluting with DMF, are 4.7× 10^3/1.00 for PSVTPA, 6.4× 10^3/1.05 for PSeVTPA, 5.9× 10^3/1.21 for PTeVTPA, and 7.8× 10^3/1.10 for PBPTPA, respectively. The formation of the C=N^+-C bond in the polymer structure has been confirmed by X-ray photoelectron spectroscopy (XPS) (Figure S2). The N1s core-level XPS spectra of these polymers showed two peaks of nitrogen functionalities at 401.69 (the N in C=N^+-C bond) and 399.60 eV (the N in C-N bond). Also, the S2p, Se3d, and Te3d core-level XPS spectra of PCVTPA showed S functionalities at 169.23 ($2P_{1/2}$) and 168.02 ($2P_{3/2}$) eV, Se functionalities at 57.51 ($3d_{3/2}$) and 56.57 ($3d_{5/2}$) eV, and Te functionalities at 584.99 ($3d_{3/2}$) and 574.69 ($3d_{5/2}$) eV. These results demonstrated the successful synthesis of both the PCVTPA and PBPTPA polymers.

From Figure 1A, it can be clearly seen that the UV-vis absorption spectrum of the PBPTPA film showed a strong absorption peak at 313 nm, followed by a broad absorption peak centered at 485 nm. The former can be assigned to TPA, whereas the latter corresponded to the typical absorption of bipyridines. Similarly, the PCVTPA film also exhibited the main absorption peaks from the TPA moieties and the chalcogenoviologen moieties. With the changes of chalcogen atoms introduced into viologen scaffolds from S to Se to Te, the absorption band assigned to the viologen moieties were found to be shifted to the longer wavelength (389 nm→415 nm→475 nm) owing to the gradually weakened electron-drawing ability from S to Se to Te. Upon excitation with laser light at 310 nm, all the samples exhibited a strong emission band that is located at 373 nm for PSVTPA, 374 nm for PSeVTPA, 375 nm for PTeVTPA, and 378 nm for PBPTPA (Figure 1B), respectively. The thermal properties of the samples were investigated by thermogravimetric analysis (TGA) in nitrogen atmosphere (Figure 1C). As a result, the onset decomposition temperature for the thermal bond cleavage of the samples was found to be 178°C for PSVTPA, 322°C for PSeVTPA, 346°C for PTeVTPA, and 353°C for PBPTPA, respectively. The thermal stability of PTeVTPA is higher than those of PSVTPA and PSeVTPA but smaller than that of PBPTPA without chalcogen atoms.

Redox potentials (versus Ag/Ag^+) of the thin film samples, which were measured in deaerated dichloromethane containing recrystallized tetrabutylammonium hexafluorophosphate ($TBAPF_6$, 0.05M) at room temperature, were found to be $E_{red\ 1,1/3}$ = −1.08 V, $E_{red\ 2,1/3}$ = −0.63 V, and $E_{red\ 3,1/3}$ = +0.82 V for PSVTPA; $E_{red\ 1,1/3}$ = −1.03 V, $E_{red\ 2,1/3}$ = −0.45 V, and $E_{red\ 3,1/3}$ = +0.75V for PSeVTPA; $E_{red\ 1,1/3}$ = −1.04 V, $E_{red\ 2,1/3}$ = −0.54 V, and $E_{red\ 3,1/3}$ = +0.79V for PTeVTPA. Similar to these materials mentioned above, redox potentials

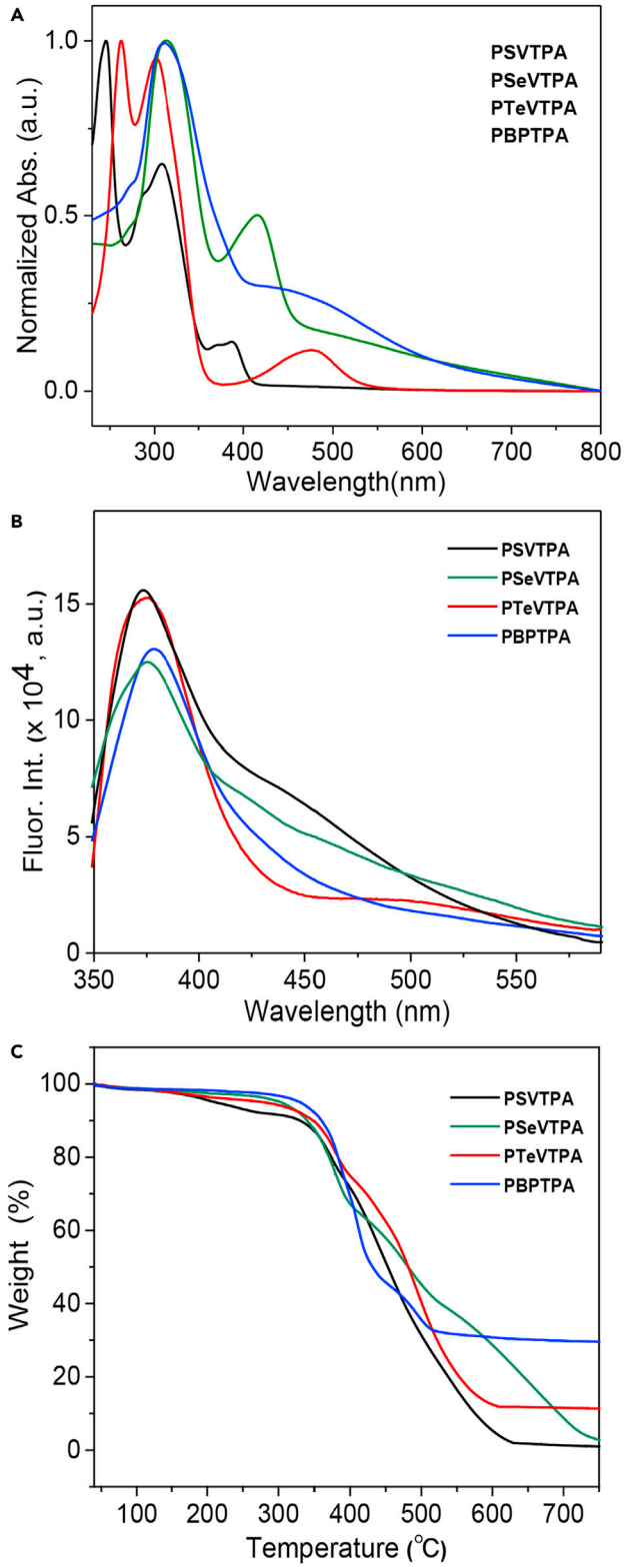

Figure 1. Basic characterization of polymers

(A) Normalized UV-vis spectra of the thin film samples.

(B) Fluorescence spectra of the samples in DMF (λ_{ex} = 310 nm).

(C) TGA curves of the samples.

(versus Ag/Ag^{+}) of the PBPTPA thin film also showed three redox potentials: $E_{red\ 1,1/3} = -1.81$ V, $E_{red\ 2,1/3} = -1.21$ V, and $E_{red\ 3,1/3} = +0.50$ V. As reported in the literature (Woodward et al., 2017; Vermeulen and Thompson, 1992; Oh et al., 2017), when a voltage is applied to Vs, these materials can exhibit apparent color changes as a result of the two-step reversible one-electron reduction that occurred in the system ($V^{2+} + e^{-} \rightarrow V^{+\cdot}$; $V^{+\cdot} + e^{-} \rightarrow V^{0}$). Similarly, PCVTPA also exhibited reversible color changes under an applied voltage. For example, the PTeVTPA film showed blue at +1 V ($PTeVTPA^{3+\cdot}$), red at 0 V ($PTeVTPA^{2+}$), green at −0.7 V ($PTeVTPA^{1+\cdot}$), and orange at −1.2 V ($PTeVTPA^{0}$), respectively. The corresponding electronic absorption spectra of the PTeVTPA film at different sweep voltages are shown in Figure S3A. In the neutral state ($PTeVTPA^{0}$), its absorption spectrum showed three main absorption peaks at 299, 363, and 556 nm. The absorption peaks of PTeVTPA at different oxidation states are located at 299, 360 (shoulder peak), 500, and 708 nm for $PTeVTPA^{1+\cdot}$; 299, 357, and 510 nm for $PTeVTPA^{2+}$; and 299, 359 (shoulder peak), 490, and 689 nm for $PTeVTPA^{3+\cdot}$, respectively. For better understanding of the absorption spectra measured experimentally, we also used time-dependent density functional theory (TD-DFT) to simulate the above electronic absorption spectra (Figure S3b). All the computational work was carried out by using B3LYP functional and def2-SVP basis set including Grimme's D3 dispersion correction (Becke-Johnson damping) (Frisch et al., 2016; Grimme et al., 2011). As a result, the predicted absorption spectra were in good coincidence with the spectra observed in the thin film sample. Furthermore, it was found that the dipole moments of PTeVTPA at different oxidation states are 12.40 Debye for $PTeVTPA^{3+\cdot}$, 18.17 Debye for $PTeVTPA^{2+}$, and 14.41 Debye for $PTeVTPA^{+\cdot}$ (Figure S4). In the neutral state ($PTeVTPA^{0}$), the calculated dipole moment is only 0.77 Debye. In general, both the intensive electron delocalization and strong dipole moment of molecule in a D-A polymer system would be able to effectively stabilize the conductive charge-transfer state and consequently produce the non-volatile nature of the high-conductivity state in an electronic memory device.

From Figure 2A, one can see a pinched hysteretic loop confined to the first and third quadrants of the I-V plane in the Al/PTeVTPA/ITO device. This result suggests that the PTeVTPA-based electronic device exhibits a typical memristive performance. When the electronic device was applied seven consecutive positive sweep voltages from 0 to 0.5 V and then back to 0 V, the observed device current was found to increase incrementally from 0.27 to 0.67 mA (read at 0.2 V). After that, the device was applied seven consecutive negative voltage sweeps of 0 V→-0.5 V→ 0 V, and the device current decreases gradually from −0.89 to −0.42 mA (read at −0.2 V). During the whole voltage sweeping processes, a smoother change of the material conductance or the device current was observed. In contrast to the above observation, for the bistable electrical switching devices reported in the literature, their switching effect usually follows steep conductance or current jumps (Liu et al., 2018; Chen et al., 2012; Lin et al., 2014). Similarly, both the Al/PSVTPA/ITO and Al/PSeVTPA/ITO devices also showed memristive effect (Figures 2B and 2C). Among these three devices, however, the changes in resistance states and the boundary between the pinched hysteretic loops observed in the Al/PTeVTPA/ITO device are much clearer than the other two devices. Unlike PCVTPA-based devices, the PBPTPA-based device displayed unstable memristive behavior (Figure 2D). These results demonstrated that the introduction of chalcogen atoms (S, Se, Te) into viologen scaffolds could greatly improve memristive performance of the resultant materials. Furthermore, by using consecutive multilevel conductance switchings, one can easily realize nonlinear transmission characteristics exhibited by a biological synapse (Figure S5), and modulation and memory of the synaptic weight, which refers to the conductance of the two-terminal device, or the strength or amplitude of a connection between two nodes in neuroscience.

The effect of film thickness on the current-voltage characteristics of the Al/PTeVTPA/ITO devices has been observed. The film thickness was varied from 37 to 85 nm and to 120 nm. As shown in Figure 3, all the devices showed a pinched hysteretic loop confined to the first and third quadrants of the I-V plane. The main difference between these devices lies in the degree of an increase (or decrease) in the magnitude of the current signal between two sweeps. For example, the device was applied seven consecutive positive voltage sweeps of 0 V→ 0.5 V→ 0 V; the current change observed between the first sweep and the seventh sweep (ΔI, read at 0.5V) was 1.9 mA (2.4 mA→4.4 mA) at 37 nm, 1.0 mA (1.1 mA→2.1 mA) at 85 nm, and 0.4 mA (1.3 mA→1.7 mA) at 120 nm, respectively. A similar change tendency was also observed when the device was applied seven consecutive negative voltage sweeps of 0 V→-0.5 V→ 0 V. These results demonstrate that the film thickness has only a little bit of influence on the change in the device current under the same experimental conditions. In contrast to the as-fabricated memristor mentioned above, for a typical bistable switching and nonvolatile rewritable memory device, the ON/OFF current ratio will increase

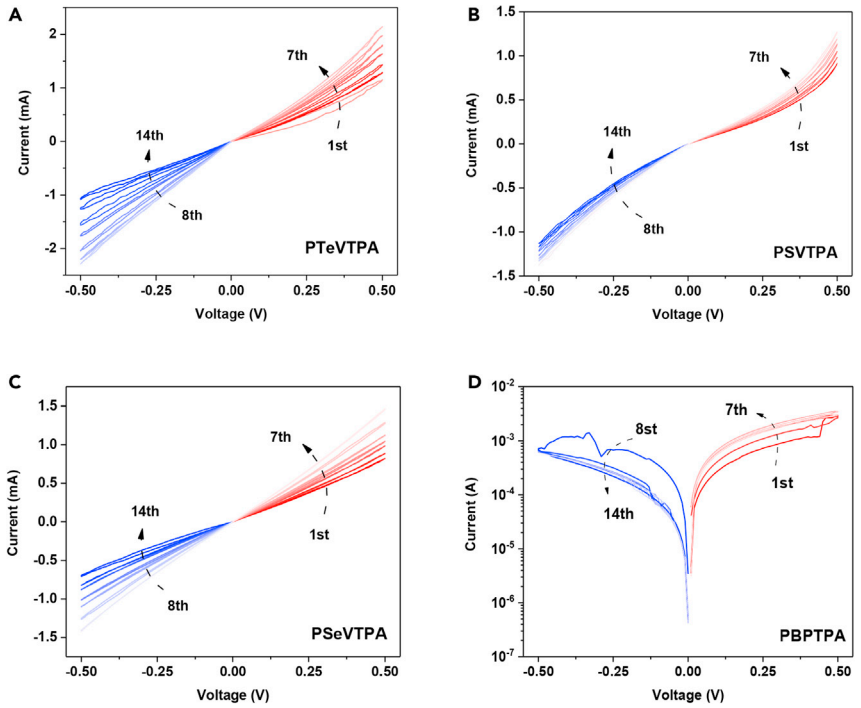

Figure 2. The current-voltage characteristics of the Al/polymer/ITO devices

(A) PTeVTPA.

(B) PSVTPA.

(C) PSeVTPA.

(D) PBPTPA.

with increasing film thickness, whereas their turn-on and turn-off voltages almost kept unchanged (Fan et al., 2017). Considering that the oxygen vacancies (oxygen anions) from the ITO electrode will diffuse into the switching layer under external electric field, we replaced the ITO electrode with the Au electrode. As shown in Figure S6, the as-fabricated Al/PTeVTPA/Au device showed almost the same memristive performance as that exhibited by the Al/PTeVTPA/ITO device. This result suggested that the migration of oxygen vacancies from the ITO electrode to the active layer has no obvious influence on the polymer-based device performance.

Resistive switching performance of the polymer memories mainly arise from changes in the intrinsic properties of the switching media. Although several switching mechanisms such as reduction-oxidation interactions, charge transfer, conformation change, and phase change have been proposed (Liu et al., 2018), less direct physical evidence is available to support these proposed mechanisms so far due to the lack of advanced *in situ* characterization and analysis tools. Therefore, it is still difficult to identify the operation mechanism of the polymer-based memory device and/or memristor at the moment (Jeong et al., 2012). In the present study, a possible operation mechanism might concern the redox process of the as-prepared polymer film under an applied electric field. At the initial stage (no voltage was applied to the device), the polymer backbone is in a positive divalent state (e.g., PTeVTPA^{2+}). When a positive sweep voltage was applied to the device, the polymer was gradually oxidized (or partially oxidized) to PTeVTPA$^{3+\cdot}$, and consequently the charge carrier concentration in the system increased, giving rise to the increase of the device current, as observed in the first quadrant of the I-V plane. When the device was applied a negative sweep voltage, with increasing the applied voltage, PTeVTPA$^{3+\cdot}$ would undergo a one-step or multiple-step electrochemical reduction reaction process (e.g., PTeVTPA$^{3+\cdot}$ → PTeVTPA^{2+} → PTeVTPA$^{1+\cdot}$ → PTeVTPA^{0}). As a result, the charge carrier concentration in the system gradually reduced, followed by the dropping of the device current with increasing the sweep times, as shown in the third quadrant of the I-V plane.

To explore the influence of stimulus frequency and duration on synaptic weights, we successfully emulated the spike-rate dependent plasticity of biological synapses (Markram et al., 1998; Li et al., 2013) by

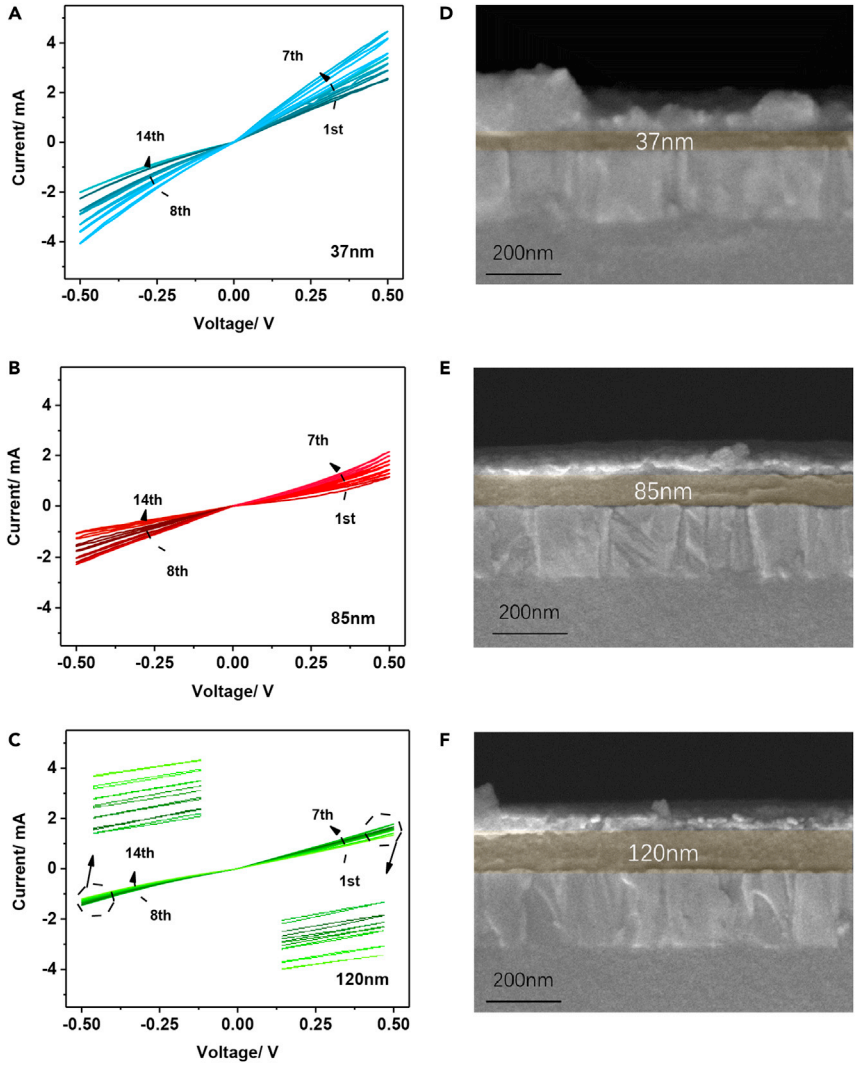

Figure 3. The effect of active layer thickness on device performance

(A–C) The effect of film thickness on the current-voltage characteristics and SEM images of the Al/PTeVTPA/ITO devices with different active layer thicknesses.

(A and D) 37 nm.

(B and E) 85 nm.

(C and F) 120 nm.

increasing the frequencies of the voltage pulses applied to the Al/PTeVTPA/ITO device (Figures 4A and 4B). During the experiments, the stimulus frequency was changed from 1 to 20 Hz, whereas the numbers of the pulse stimulations was fixed at a constant of 10. As seen from Figure 4A, the more frequently the device acting as biological synapse was being stimulated, the higher the device currents observed in this study became. It was also found that, at the frequency of 1 or 2 Hz, the device current changes with 10 pulse stimulations were very small. With further increasing the frequency, the observed current changes started to become more apparent or remarkable. At a frequency of 20 Hz and the stimulation numbers of 10, the device current changes reached up to 51.99 μA when compared with the stimulation number of 1. These results suggest that the as-prepared memristor can serve as a high-pass filter. Figure 4C shows the device current as a function of the pulse durations at a frequency of 1 Hz and the stimulation numbers of 5, suggesting the good stability of the device. Considering that the sub-threshold potentiation in neurons is associated with both paired pulse facilitation (PPF) and short-term synaptic plasticity (STP), we also established such functionality in our device. From Figure 4D, it can be seen that the PPF shows two

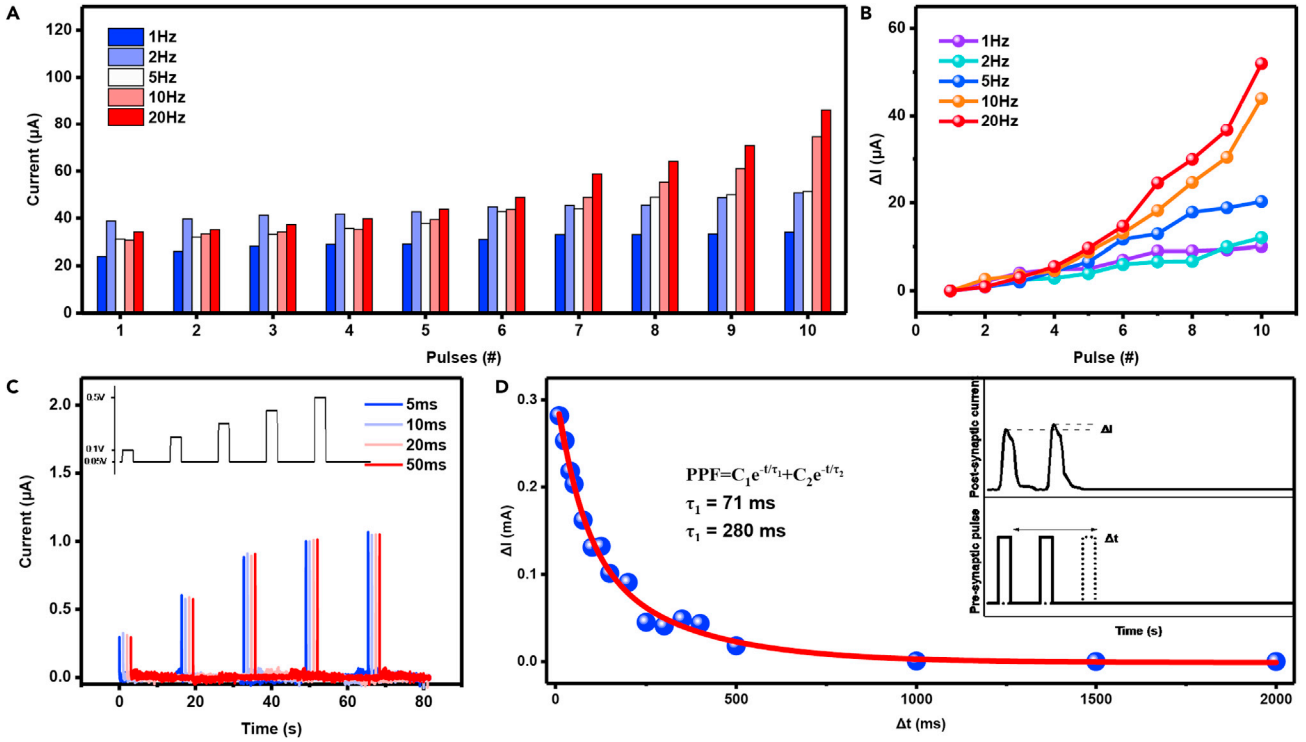

Figure 4. Frequency-dependent synaptic potentiation of the Al/PTeVTPA/ITO memristor

(A) Evolution of the device current.

(B) Evolution of the device current change (ΔI = In- I1) at different frequencies.

(C) Current with five pulse stimulations at different pulse durations (inset: schematic diagram of the applied pulse).

(D) Short-term potentiation and paired pulse facilitation. The amount by which the synaptic weight is temporarily modified depends on the time interval between two short pulses. An exponential fit is applied to obtain two characteristic timescales. The inset is a schematic diagram of how such biasing is typically realized.

characteristic timescales (van de Burgt et al., 2017), with τ_1 of 71 ms and τ_2 of 280 ms. These two values are very close to those exhibited by biological synapses (Zucker and Regehr, 2002).

The synaptic potentiation and depression, which are regarded as the neurobiological basis of the brain memory functions, may be realized through action potential spikes. When the device was applied the consecutive negative voltage pulses or positive stimuli, respectively, synaptic weight can be effectively depressed or potentiated (Figure 5A). The synaptic potentiation and relaxation processes are found to compete with each other during the biological stimuli. Figure 5B showed the retention curves for synaptic weight at different numbers of identical voltage pulse stimulations, from which one can see that the synaptic weight undergoes the fast decay at the beginning and then gradually tends to fatten out. This result implies that the numbers of identical voltage pulse stimulations with same amplitude, period, and duration can greatly influence the memory loss or retention performance of the device. Basically, the human memory mainly comes from STP and long-term potentiation/plasticity (LTP). Long-term memory can be sustained for a long time (e.g., several days, several months, even several years), whereas short-term memory only lasts for a very short time (e.g., several seconds or minutes). Even an accidental electrical shock or decay rapidly with time may easily interrupt or destroy short-term memory. As shown in Figure 5C, with increasing the pulse stimulation numbers the relaxation time constant (τ) was changed from 4.51 s@10 pulses to 4.98 s@20 pulses to 6.81 s@30 pulses to 7.40 s@40 pulses to 9.35 s@50 pulses and to 10.36 s@60 pulses. This finding makes the transition from short-term memory to long-term memory possible in our device. And more a "learning → forgetting → re-learning" process shown in human daily life has been successfully explored in this study (Figures 5D–5G). When a stimulation of 50 consecutive voltage pulses was applied to the device, the device current was found to increase gradually with the increase of the pulse numbers (Figure 5D). This is similar to a "learning" process observed during the human learning. Once the power was cut off, the device current dropped gradually to an intermediate state within 200 s (Figure 5E). This process can

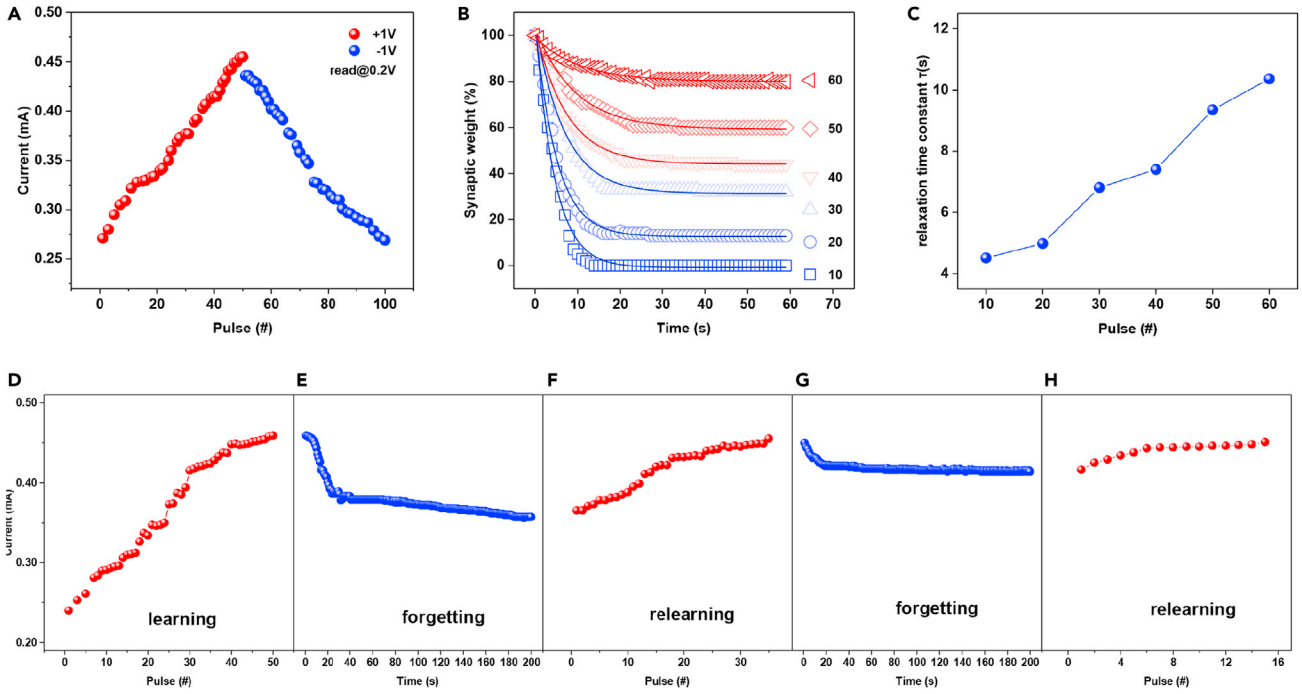

Figure 5. Simulation of human brain memory behavior

(A) The current in response to a series of positive and negative voltage stimulations showing the respective potentiation and depression of the device synaptic connection.

(B) Experimental (symbols) and fitted (solid lines) memory retention performance after being subjected to different numbers of identical voltage pulse stimulations.

(C) Evolution of the relaxation time constant (τ) and the stabilized synaptic weight (I0) along with the stimulating numbers. $I(t) = I_0+Aexp(-t/\tau)$.

(D–H) demonstration of the "learning-forgetting-relearning" process. The amplitude, duration, and period of the voltage pulses are 1 V, 10 ms, and 1 s, respectively. The current responses are monitored with a small voltage of 0.2 V.

be regarded as a "forgetting" process. And then we applied a stimulation of 35 consecutive pulses to the device again, and the current returned to its end level from the first learning stage (Figure 5F). Such a "re-learning" process is similar to the transition process from STP to LTP, by which the human memory capability can be significantly strengthened. Afterward, the as-fabricated device went through a "re-forgetting" process again (Figure 5G). By comparison with the device current detected at the end of the first "forgetting" process, which is about 0.36 mA, the device current observed at the end of the "re-forgetting" process reached up to 0.41 mA, much higher than that of the former. This suggests that the "re-forgetting" speed slows down greatly when compared with the first "forgetting" speed. Surprisingly, it only took 15 voltage pulses for the device current to be recovered to the same higher level as that shown at the end level from the first learning stage (Figure 5H). These results demonstrated that the voltage pulses applied to the device would become fewer and fewer with an increasing number of "re-learning" processes.

From the above discussion, we can see that our device shows a consecutive resistive switching effect at any device current levels. This result is very interesting and can be used to implement arithmetic addition, subtraction, multiplication, and division. When a stimulation of consecutive voltage pulses was applied to the device, as shown in Figure 6A, whatever positive sweeping or negative sweeping, the relationship between the pulse numbers and the device currents read at $\pm$0.5V is perfectly linear. This relationship guarantees the normal operation of the device as a decimal abacus. It was also found that the pinched hysteretic loops shown in Figures 2A–2C are highly symmetric. For calibration, an X-X = 0 operation is carried out in pulse mode to guarantee the calculating accuracy (Figure 6B). After a stimulation of 10 consecutive positive pulses (0.5 V and 10 ms) was applied to the device, the observed device current reached 0.43 mA. As such, when a current of ~0.43 mA is read, the number 10 will be counted in future calculation. By setting the device current of $\leq$0.2 mA as the initial state of the device, the decimal numbers of 0–10 can be indexed proportionally. When a subsequent stimulation of 10 consecutive negative pulses was applied, the device current got back to the initial state again. With such an operation, one can easily realize the subtraction

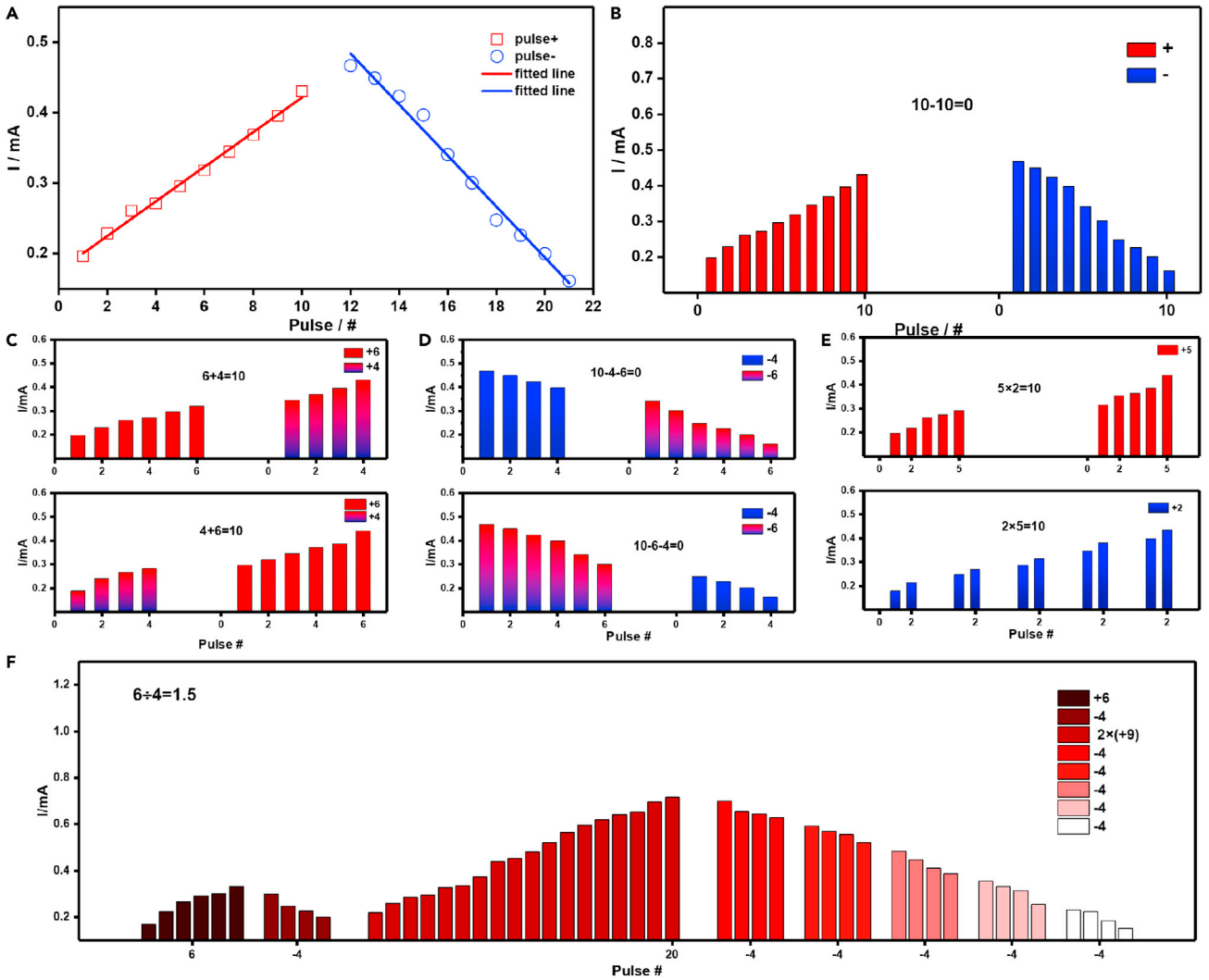

Figure 6. Demonstration of arithmetic computing with the Al/PTeVTPA/ITO memristor

(A) Linear relationship between the device currents read at ± 0.5 V and voltage sweeping numbers.

(B) Calibration of the memristor with the operation of 10–10 = 0 for decimal arithmetic calculations.

(C) Commutative addition conducted with the PTeVTPA device.

(D) Subtraction conducted with the PTeVTPA device.

(E) Multiplication conducted with the PTeVTPA device.

(F) Fractional division conducted with the PTeVTPA device.

operation of 10–10 = 0 and calibrate the as-fabricated device for accurate decimal arithmetic operations. In this device, the application of positive voltages, which can result in the increase of the device current, was used to make addition operations, whereas the negative voltages applied to the device correspond to the subtraction function of an ''abacus.'' By monitoring the current changes with respect to the initial state of the device, the quantity of the input pulse stimuli can be counted.

The application of a succession of six consecutive positive pulses (0.5 V and 10 ms) followed by an extra train of four consecutive positive pulses with the same duration and amplitude as those of the former produces a device current of ~0.43 mA, which exactly confirms 6 + 4 = 10 (Figure 6C). When we reverse the sequence of the two sets of input pulse signals, the device current also reached ~0.43 mA under the same experimental conditions. These results verify such a commutative law that X + Y=Y + X (6 + 4 = 4 + 6 = 10). After the pre-loading of 10 positive pulses (0.5 V and 10 ms), which gives a device current of ~0.43 mA, the sequential application of four consecutive negative pulses and a following train of six consecutive negative pulses

resulted in that the device current is down back to the initial state again (Figure 6D). This confirmed 10−6−4 = 0. Reversing the loading order of the input signals can also reduce the device current to the value at the initial state (10−4−6 = 0), which confirms that X−Y−Z = X−Z−Y (10−6−4 = 10−4−6 = 0). These findings demonstrated the commutative subtraction operation. Similarly, the accumulative addition operation-based multiplication also obeys the commutative law (Figure 6E). The result obtained from the application of two sets of five positive pulses is the same as that from the application of five sets of two positive pulses, assuring that X×Y=Y×X (2 × 5 = 5 × 2 = 10). The fractional division is based on the combination of the subtraction and addition operations. For example, we can carry out the division operation of 6÷4 with our device (Figure 6F). The device was first reset to the initial state, and then was applied six consecutive positive voltage pulses, followed by another series of four negative pulses, to perform 6−4. As a result, a remainder of 2 and an integer quotient of 1 were achieved. Considering the remainder 2 is smaller than the divisor 4, we added two series of 9 positive voltage pulses to the device to replace 2 with "2 + 2×9" (2 × 10). Subsequently repeated subtraction of −4 for five times (20− 4− 4− 4− 4− 4) made the device current back to the initial state again. The fractional division calculation was then terminated. These results demonstrate that the decimal number of 5 was at the tenths position and the quotient of 6÷4 = 1.5 (1 + 0.5).

Conclusions

A proof-of-concept PCVTPA-based polymer memristor with a configuration of Al/PCVTPA/ITO exhibited excellent history-dependent memristive switching and multilevel storage performance. Associated with the unique memristive behavior, the as-fabricated device can be used to not only emulate the human's learning and memorizing functions but also execute decimal arithmetic operations of addition, subtraction, multiplication, and division. These results demonstrated that the PCVTPA polymer showed a great potential in constructing high-performance intelligent computing system in the near future.

Limitations of the study

This work is mainly focused on the design and synthesis of new chalcogenoviologen and triphenylamine-based alternative copolymer for constructing high-performance synaptic biomimicking and neuromorphic computing system. This material shows excellent history-dependent memristive switching and multilevel storage performance. The memristive performance of the polymers mainly arises from changes in the intrinsic properties of the switching media. In contrast to the inorganic materials-based memory and memristor, the proposed main switching mechanisms of the polymer-based devices are reduction-oxidation interactions, charge transfer, conformation change, and phase change. However, less direct physical evidence is available to support these proposed mechanisms so far owing to the lack of advanced *in situ* characterization and analysis tools. Therefore, it is still difficult to identify the operation mechanism of the polymer-based memristors at the moment. Future work should be focused on the design of new high-performance conjugated polymer functional materials for memristors, exploration of the operation mechanism, and determination of the relationship between the structural parameters and the memristive response while seeking to optimally combine materials and devices.

STAR★METHODS

Detailed methods are provided in the online version of this paper and include the following:

- KEY RESOURCES TABLE
- RESOURCE AVAILABILITY
  - Lead contact
  - Materials availability
  - Data and code availability
- EXPERIMENTAL MODEL AND SUBJECT DETAILS
- METHOD DETAILS
  - Measurements and instrument
  - Synthetic procedure
  - Device fabrication and characterization
  - Structural modeling
- QUANTIFICATION AND STATISTICAL ANALYSIS
- ADDITIONAL RESOURCES

SUPPLEMENTAL INFORMATION

Supplemental information can be found online at https://doi.org/10.1016/j.isci.2021.103640.

ACKNOWLEDGMENTS

The authors acknowledge the financial support from the National Natural Science Foundation of China (51961145402, 51333002, and 51973061), Natural Science Foundation of Shanghai (19ZR1413100), Shanghai Rising-Star Program (21QA1402100), and the Fundamental Research Funds for the Central Universities (50321041918013). We also thank the Center for Information Services and High Performance Computing (ZIH) at TU Dresden for generous allocations of computing resources. M.E.E.-K. wants to thank the Academy of Scientific Research and Technology (ASRT, Egypt) for financial support.

AUTHOR CONTRIBUTIONS

Y.C., Z.Z., and B.Z. conceived the idea. Z.Z., Q.C., K.W., J.L., and M.E.E.-K. synthesized and characterized all the materials. Y.F. simulated the electronic absorption spectra of the samples. Y.C. wrote the manuscript. All authors discussed the experimental results.

DECLARATION OF INTERESTS

The authors declare no competing interests.

Received: August 30, 2021
Revised: November 15, 2021
Accepted: December 14, 2021
Published: January 21, 2022

REFERENCES

Bandyopadhyay, A., Sahu, S., and Higuchi, M. (2011). Tuning of nonvolatile bipolar memristive switching in Co (III) polymer with an extended azo aromatic ligand. J. Am. Chem. Soc. *133*, 1168–1171. https://doi.org/10.1021/ja106945v.

Chen, Y., Zhang, B., Liu, G., Zhuang, X., and Kang, E.T. (2012). Graphene and its derivatives: switching ON and OFF. Chem. Soc. Rev. *41*, 4688–4707. https://doi.org/10.1039/c2cs35043b.

Chen, Y., Liu, G., Wang, C., Zhang, W., Li, R.W., and Wang, L. (2014). Polymer memristor for information storage and neuromorphic applications. Mater. Horiz. *1*, 489–506. https://doi.org/10.1039/c4mh00067f.

Choi, S., Jang, S., Moon, J.H., Kim, J.C., Jeong, H.Y., Jang, P., Lee, K., and Wang, G. (2018). A self-rectifying TaO y/nanoporous TaO x memristor synaptic array for learning and energy-efficient neuromorphic systems. NPG Asia Mater. *10*, 1097–1106. https://doi.org/10.1038/s41427-018-0101-y.

Choi, S., Yang, J., and Wang, G. (2020). Emerging memristive artificial synapses and neurons for energy-efficient neuromorphic computing. Adv. Mater. *32*, 2004659. https://doi.org/10.1002/adma.202004659.

Ding, J., Zheng, C., Wang, L., Lu, C., Zhang, B., Chen, Y., Li, M., Zhai, G., and Zhuang, X. (2019). Viologen-inspired functional materials: synthetic strategies and applications. J. Mater. Chem. A *7*, 23337–23360. https://doi.org/10.1039/c9ta01724k.

Ego, C., Grimsdale, A.C., Uckert, F., Yu, G., Srdanov, G., and Müllen, K. (2002). Triphenylamine-substituted polyfluorene—a stable blue-emitter with improved charge injection for light-emitting diodes. Adv. Mater. *14*, 809–811. https://doi.org/10.1002/1521-4095(20020605)14:11<809::AID-ADMA809>3.0.CO;2-8.

El-Khouly, M.E., Chen, Y., Zhuang, X., and Fukuzumi, S. (2009). Long-lived charge-separated configuration of a push− pull archetype of disperse red 1 end-capped poly [9, 9-bis (4-diphenylaminophenyl) fluorene]. J. Am. Chem. Soc. *131*, 6370–6371. https://doi.org/10.1021/ja901588f.

Fan, F., Zhang, B., Cao, Y., and Chen, Y. (2017). Solution-processable poly(*N*-vinyl- carbazole)-covalently grafted MoS_2 nanosheets for nonvolatile rewritable memory devices. Nanoscale *9*, 2449–2456. https://doi.org/10.1039/c6nr09241a.

Fang, Q., and Yamamoto, T. (2004). New alternative copolymer constituted of fluorene and triphenylamine units with a Tunable− CHO group in the side chain. Quantitative transformation of the− CHO group to− CH CHAr groups and optical and electrochemical properties of the polymers. Macromolecules *37*, 5894–5899. https://doi.org/10.1021/ma0359133.

Frisch, M.J., Trucks, G.W., Schlegel, H.B., Scuseria, G.E., Robb, M.A., Cheeseman, J.R., Scalmani, G., Barone, V., Petersson, G.A., Nakatsuji, H., et al. (2016). Gaussian 16, Revision C.01 (Gaussian, Inc.).

Grimme, S., Ehrlich, S., and Goerigk, L. (2011). Effect of the damping function in dispersion corrected density functional theory. J. Comput. Chem. *32*, 1456–1465. https://doi.org/10.1002/jcc.21759.

Jeong, D.S., Thomas, R., Katiyar, R.S., Scott, J.F., Kohlstedt, H., Petraru, A., and Hwang, C.S. (2012). Emerging memories: resistive switching mechanisms and current status. Rep. Prog. Phys. *75*, 076502. https://doi.org/10.1088/0034-4885/75/7/076502.

Kim, S., Jung, S., Kim, M.H., Chen, Y.C., Chang, Y.F., Ryoo, K.C., Cho, S., Lee, J.-H., and Park, B.G. (2018). Scaling effect on silicon nitride memristor with highly doped Si substrate. Small *14*, 1704062. https://doi.org/10.1002/smll.201704062.

Kortz, C., Hein, A., Ciobanu, M., Walder, L., and Oesterschulze, E. (2019). Complementary hybrid electrodes for high contrast electrochromic devices with fast response. Nat. Commun. *10*, 1–7. https://doi.org/10.1038/s41467-019-12617-4.

Li, S., Zeng, F., Chen, C., Liu, H., Tang, G., Gao, S., and Guo, D. (2013). Synaptic plasticity and learning behaviours mimicked through Ag interface movement in an Ag/conducting polymer/Ta memristive system. J. Mater. Chem. C *1*, 5292–5298. https://doi.org/10.1039/c3tc30575a.

Li, C., Han, L., Jiang, H., Jang, M., Lin, P., Wu, Q., Barnell, M., Yang, J., Xin, H., and Xia, Q. (2017). Three-dimensional crossbar arrays of self-rectifying Si/SiO2/Si memristors. Nat. Commun. *8*, 156661097–156661106. https://doi.org/10.1038/ncomms15666.

Li, G., Xu, L., Zhang, W., Zhou, K., Ding, Y., Liu, F., He, X., and He, G. (2018). Narrow-bandgap chalcogenoviologens for electrochromism and visible-light-driven hydrogen evolution. Angew. Chem. Int. Ed. *57*, 4897–4901. https://doi.org/10.1002/anie.201711761.

Li, G., Zhang, B., Wang, J., Zhao, H., Ma, W., Xu, L., Zhang, W., Zhou, K., and He, G. (2019). Electrochromic poly (chalcogenoviologen) s as anode materials for high-performance organic radical lithium-ion batteries. Angew. Chem. Int. Ed. *131*, 8556–8561. https://doi.org/10.1002/anie.201903152.

Lin, W.-P., Liu, S.-J., Gong, T., Zhao, Q., and Huang, W. (2014). Polymer-based resistive memory materials and devices. Adv. Mater. *26*, 570–606. https://doi.org/10.1002/adma.201302637.

Ling, Q.-D., Liaw, D.-J., Zhu, C., Chan, D.S.-H., Kang, E.-T., and Neoh, K.-G. (2008). Polymer electronic memories: materials, devices and mechanisms. Prog. Polym. Sci. *33*, 917–978. https://doi.org/10.1016/j.progpolymsci.2008.08.001.

Lipke, M.C., Cheng, T., Wu, Y., Arslan, H., Xiao, H., Wasielewski, M.R., Goddard, W.A., and Stoddart, J.F. (2017). Size-matched radical multivalency. J. Am. Chem. Soc. *139*, 3986–3998. https://doi.org/10.1021/jacs.6b09892.

Liu, C.L., and Chen, W.C. (2011). Donor–acceptor polymers for advanced memory device applications. Polym. Chem. *2*, 2169–2174. https://doi.org/10.1039/C1PY00189B.

Liu, G., Wang, C., Zhang, W., Pan, L., Zhang, C., Yang, X., Fan, F., Chen, Y., and Li, R. (2016). Organic biomimicking memristor for information storage and processing applications. Adv. Electron. Mater. *2*, 1500298. https://doi.org/10.1002/aelm.201500298.

Liu, G., Chen, Y., Gao, S., Zhang, B., Li, R.W., and Zhuang, X. (2018). Recent advances in resistive switching materials and devices: from memories to memristors. Eng. Sci. *4*, 4–43. https://doi.org/10.30919/es8d779.

Markram, H., Gupta, A., Uziel, A., Wang, Y., and Tsodyks, M. (1998). Information processing with frequency-dependent synaptic connections. Neurobiol. Learn. Mem. *70*, 101–112. https://doi.org/10.1006/nlme.1998.3841.

McFarlane, T., Bandera, Y., Grant, B., Zdyrko, B., Foulger, S.H., Vilčáková, J., Sáha, P., and Pfleger, J. (2020). Carbazole derivatized n-alkyl methacrylate polymeric memristors as flexible synaptic substitutes. Adv. Electron. Mater. *6*, 2000042. https://doi.org/10.1002/aelm.202000042.

Mi, Z., Yang, P., Wang, R., Unruangsri, J., Yang, W., Wang, C., and Guo, J. (2019). Stable radical cation-containing covalent organic frameworks exhibiting remarkable structure-enhanced photothermal conversion. J. Am. Chem. Soc. *141*, 14433–14442. https://doi.org/10.1021/jacs.9b07695.

Oh, H., Seo, D.G., Yun, T.Y., Kim, C.Y., and Moon, H.C. (2017). Voltage-tunable multicolor, sub-1.5 V, flexible electrochromic devices based on ion gels. ACS Appl. Mater. Interfaces *9*, 7658–7665. https://doi.org/10.1021/acsami.7b00624.

Pincella, F., Camorani, P., and Erokhin, V. (2011). Electrical properties of an organic memristive system. Appl. Phys. A *104*, 1039–1046. https://doi.org/10.1007/s00339-011-6399-8.

Ren, Y., Lin, W.C., Ting, L.Y., Ding, G., Yang, B., Yang, J.Q., Chou, H.H., Han, S.T., and Zhou, Y. (2020). Iridium-based polymer for memristive devices with integrated logic and arithmetic applications. J. Mater. Chem. C *8*, 16845–16857. https://doi.org/10.1039/d0tc03800h.

Sluysmans, D., Zhang, L., Li, X., Garci, A., Stoddart, J.F., and Duwez, A.S. (2020). Viologen tweezers to probe the force of individual donor–acceptor π-interactions. J. Am. Chem. Soc. *142*, 21153–21159. https://doi.org/10.1021/jacs.0c10339.

Stolar, M., Reus, C., and Baumgartner, T. (2016). Xylene-bridged phosphaviologen oligomers and polymers as high-performance electrode-modifiers for Li-ion batteries. Adv. Energy Mater. *6*, 1600944. https://doi.org/10.1002/aenm.201600944.

Strukov, D.B., Snider, G.S., Stewart, D.R., and Williams, R.S. (2008). The missing memristor found. Nature *453*, 80–83. https://doi.org/10.1038/nature06932.

Sun, B., Xiao, M., Zhou, G., Ren, Z., Zhou, Y.N., and Wu, Y.A. (2020). Nonezero-crossing current-voltage hysteresis behavior in memristive system. Mater. Today Adv. *6*, 100056. https://doi.org/10.1016/j.mtadv.2020.100056.

van de Burgt, Y., Lubberman, E., Fuller, E.J., Keene, S.T., Faria, G.C., Agarwal, S., and Salleo, A. (2017). A non-volatile organic electrochemical device as a low-voltage artificial synapse for neuromorphic computing. Nat. Mater. *16*, 414–418. https://doi.org/10.1038/nmat4856.

van De Burgt, Y., Melianas, A., Keene, S.T., Malliaras, G., and Salleo, A. (2018). Organic electronics for neuromorphic computing. Nat. Electron. *1*, 386–397. https://doi.org/10.1038/s41928-018-0103-3.

Vermeulen, L.A., and Thompson, M.E. (1992). Stable photoinduced charge separation in layered viologen compounds. Nature *358*, 656–658. https://doi.org/10.1038/358656a0.

Wan, F., Wang, Q., Harumoto, T., Gao, T., Ando, K., Nakamura, Y., and Shi, J. (2020). Truly electroforming-free memristor based on TiO2-CoO phase-separated oxides with extremely high uniformity and low power consumption. Adv. Funct. Mater. *30*, 2007101. https://doi.org/10.1002/adfm.202007101.

Wang, C., Liu, G., Chen, Y., Liu, S., Chen, Q., Li, R., and Zhang, B. (2014). Dithienopyrrole-/benzodithiophene-based donor-acceptor polymers for memristor. ChemPlusChem *79*, 1263. https://doi.org/10.1002/cplu.201402206.

Wang, C., Liu, G., Chen, Y., Li, R.W., Zhang, W., Wang, L., and Zhang, B. (2015). Synthesis and nonvolatile memristive switching effect of a donor–acceptor structured oligomer. J. Mater. Chem. C *3*, 664–673. https://doi.org/10.1039/c4tc02285h.

Woodward, A.N., Kolesar, J.M., Hall, S.R., Saleh, N.-A., Jones, D.S., and Walter, M.G. (2017). Thiazolothiazole fluorophores exhibiting strong fluorescence and viologen-like reversible electrochromism. J. Am. Chem. Soc. *139*, 8467–8473. https://doi.org/10.1021/jacs.7b01005.

Yang, X., Cheng, Q., Monnier, V., Charles, L., Karoui, H., Ouari, O., Gigmes, D., Wang, R., Kermagoret, A., and Bardelang, D. (2021). Guest exchange by a partial energy ratchet in water. Angew. Chem. Int. Ed. *133*, 6691–6697. https://doi.org/10.1002/anie.202014399.

Zhang, P., Zhu, F., Wang, F., Wang, J., Dong, R., Zhuang, X., Schmidt, O.G., and Feng, X. (2017). Stimulus-responsive micro-supercapacitors with ultrahigh energy density and reversible electrochromic window. Adv. Mater. *29*, 1604491. https://doi.org/10.1002/adma.201604491.

Zhang, B., Wang, C., Wang, L., and Chen, Y. (2018). Macrocyclic triphenylamine-based push–pull type polymer memristive material: synthesis and characterization. J. Mater. Chem. C *6*, 4023–4029. https://doi.org/10.1039/c8tc00524a.

Zhang, B., Chen, W., Zeng, J., Fan, F., Gu, J., Chen, X., Yan, L., Xie, G., Liu, S., and Yan, Q. (2021). 90% yield production of polymer nano-memristor for in-memory computing. Nat. Commun. *12*, 1984. https://doi.org/10.1038/s41467-021-22243-8.

Zhang, B., Fan, F., Xue, W., Liu, G., Fu, Y., Zhuang, X., Xu, J., Li, R., and Chen, Y. (2019). Redox gated polymer memristive processing memory unit. Nat. Commun. *10*, 736. https://doi.org/10.1038/s41467-019-08642-y.

Zhang, M., Ma, C., Du, D., Xiang, J., Yao, S., Hu, E., Liu, S., Tong, Y., Wong, W., and Zhao, Q. (2020). Donor–acceptor metallopolymers containing ferrocene for brain inspired memristive devices. Adv. Electron. Mater. *6*, 2000841. https://doi.org/10.1002/aelm.202000841.

Zhou, G., Sun, B., Hu, X., Sun, L., Zou, Z., Xiao, B., Qiu, W., Wu, B., Li, J., Han, J., et al. (2021). Negative photoconductance effect: an extension function of the TiOx-based memristor. Adv. Sci. *8*, 2003765. https://doi.org/10.1002/advs.202003765.

Zucker, R.S., and Regehr, W.G. (2002). Short-term synaptic plasticity. Annu. Rev. Physiol. *64*, 355–405. https://doi.org/10.1146/annurev.physiol.64.092501.114547.

STAR★METHODS

KEY RESOURCES TABLE

REAGENT or RESOURCE	SOURCE	IDENTIFIER
Chemicals, peptides, and recombinant proteins		
3-Bromopyridine (AR)	Aladdin	CAS:626-55-1
4,4′-bipyridine (98%, AR)	Aladdin	CAS:553-26-4
Diisopropylamine (>99%, GC)	Aladdin	CAS:108-18-9
Phosphorus tribromide (99%, AR)	Aladdin	CAS:7789-60-8
Phosphorus oxychloride (98%, AR)	Aladdin	CAS:10025-87-3
Copper chloride (98%, AR)	Aladdin	CAS:7447-39-4
Triphenylamine (98%, AR)	Aladdin	CAS:603-34-9
Selenium powder (99.999% (metals basis), 200mesh)	Adamas-beta	CAS:7782-49-2
Sulfuryl chloride (98%, RG)	Adamas-beta	CAS:7791-25-5
Trifluoromethanesulfonic acid (99%, AR)	J&K	CAS:1493-13-6

RESOURCE AVAILABILITY

Lead contact

Further information and requests for resources and reagents should be directed to and will be fulfilled by the lead contact, Prof. Yu Chen (chentangyu@yahoo.com; yuchenavh@ecust.edu.cn).

Materials availability

All materials generated in this study are available from the lead contact.

Data and code availability

This study does not generate data sets/code.

EXPERIMENTAL MODEL AND SUBJECT DETAILS

This study does not use experimental models typical in the life sciences.

METHOD DETAILS

All reactions were carried out under dry nitrogen atmosphere by using standard Schlenk techniques. 3-Bromopyridine and diisopropylamine were redistilled before use. Copper chloride was dried under vacuum overnight at 200°C before use. The other analytically pure chemicals were used without further purification. Organic solvents were purchased from purified, dried, and distilled under dry argon. About the synthetic procedure, measurements, instruments, device fabrication and characterization, and structural modeling are listed as follows.

Measurements and instrument

Ultraviolet/visible (UV/Vis) absorption spectra were measured on a Shimadzu UV-2540 spectrophotometer. A HORIBA JOBIN YVON Fluoromax-4 spectrofluorometer (HORIBA Scientific, France) was used to record the steady-state fluorescence spectra. Thermogravimetric analyses (TGA) of all samples were measured using a Perkin-Elmer Pyris1 thermogravimetric analyzer with a heating rate of 20°C min^{-1} under N_2 atmosphere. Nuclear magnetic resonance (NMR) spectra were recorded on a Bruker 400 spectrometer at a resonance frequency of 400 MHz for ^1H in deuterated solution with a tetramethylsilane (TMS) as a reference for the chemical shifts. Cyclic voltammetry (CV) measurements were performed on a model CHI 650D electrochemical workstation using tetrabutylammonium hexafluorophosphate (0.05M) in DCM as the supporting electrolyte, a platinum disk as working electrode, an Ag/AgCl electrode as reference, and a Pt wire as counter electrode. Fourier transform infrared (FT-IR) spectra were recorded using Spectrum 100 spectrophotometer (Perkin Elmer, Inc., USA). X-ray photoelectron spectroscopy (XPS) measurements were carried out on a Kratos AXIS HSi spectrometer with a monochromatized Al KR X-ray source (1486.6 eV photons) at a

constant dwell time of 100 ms and pass energy of 40 eV. The anode voltage and current were set at 15 kV and 10 mA, respectively. The pressure in the analysis chamber was maintained at 5×10^{-8} Torr or lower during each measurement. The number-average (Mn) and weight-average (Mw) molecular weights of the polymers were determined with a Gel Permeation Chromatograph PL-GPC50 using a polystyrene standards eluting with DMF. Field emission scanning electron microscopy (FE-SEM) images were tested on 500-300000/GeminiSEM 500.

Synthetic procedure

Synthesis of 3,3′-dibromo-4,4′-bipyridine(1). To a stirred solution of the newly synthesized lithium diisopropylamide (LDA, 2 M in THF, 30 mmol) in THF was added dropwise 3-bromopyridine (2.9 mL, 30 mmol) at -94°C. The deep orange solution was then stirred for additional one hour at -94°C and anhydrous $CuCl_2$ (9.8 g, 73 mmol) added. After stirring overnight at the same temperature, the reaction mixture was allowed to warm to the room temperature. The solvent was removed under reduced pressure. The residual brown solid was taken up in H_2O (30 mL), NH_4OH (25 %, 30 mL) and NH_4Cl (sat., 30 mL). The mixture was extracted several times with $CHCl_3$ (50 mL each time), the combined organic phases were dried over anhydrous Na_2SO_4 and concentrated to give a brown oil, which was purified by column chromatography (SiO_2, petroleum ether/ethyl acetate, 5:1) to give 2.03 g (43 %) of white powder. ^{1}H-NMR (400 MHz, $CDCl_3$): δ/ppm=8.88 (s, 2H), 8.65 (d, 2H), 7.18 (d, 2H).

Synthesis of thieno[2,3-c:5,4-c′]bipyridine(2a). To a stirred solution of 3,3′-dibromo-4,4′-bipyridine (628 mg, 2.0 mmol) in dry THF (60 mL) was added dropwise a solution of n-BuLi (2.5 M in hexanes, 1.68 mL, 4.2 mmol) via syringe at -94°C. After stirring for 1 hour at the same temperature, S_2Cl_2 (284 mg, 2.1 mmol) was added dropwise to the above solution. The reaction mixture was then allowed to warm to the room temperature and stirring was continued overnight. After evaporation of the solvent under reduced pressure, the residue was taken up in H_2O (30 mL), NH_4OH (25 %, 30 mL) and NH_4Cl (sat., 30 mL). The mixture was extracted several times with $CHCl_3$ (50 mL each time), the combined organic phases were dried over anhydrous Na_2SO_4 and concentrated to give a brown oil, which was purified by column chromatography (SiO_2, petroleum ether/ethyl acetate, 2:1) to give 150 mg (40 %) of light yellow solid. ^{1}H-NMR (400 MHz, $CDCl_3$): δ/ppm=9.30 (s, 2H), 8.76 (d, 2H), 8.14 (d, 2H).

Synthesis of selenopheno[2,3-c:5,4-c′]bipyridine(2b). To a stirred solution of 3,3′-dibromo-4,4′-bipyridine (628 mg, 2.0 mmol) in dry THF (60 mL) was added dropwise a solution of n-BuLi (2.5 M in hexanes, 1.68 mL, 4.2 mmol) via syringe at -94°C. After stirring for 1 hour at the same temperature, $SeCl_2$ (315 mg, 2.1 mmol) in THF (5 mL) was added dropwise to the above solution. The reaction mixture was then allowed to warm to the room temperature and stirring was continued overnight. After evaporation of the solvent under reduced pressure, the residue was taken up in H_2O (30 mL), NH_4OH (25 %, 30 mL) and NH_4Cl (sat., 30 mL). The mixture was extracted several times with $CHCl_3$ (50 mL each time), the combined organic phases were dried over anhydrous Na_2SO_4 and concentrated to give a brown oil, which was purified by column chromatography (SiO_2, petroleum ether/ethyl acetate, 1:1) to give 89 mg (20 %) of light yellow solid. ^{1}H-NMR (400 MHz, $CDCl_3$): δ/ppm=9.30 (s, 2H), 8.76 (d, 2H), 8.14 (d, 2H).

THF solution of $SeCl_2$ was prepared. Typically, SO_2Cl_2 (0.270 g, 2.0 mmol) was added dropwise to selenium powder (0.158 g, 2.0 mmol) at room temperature. After stirring for 10 minutes, 5 mL of THF was added to the above mixture. The solution was then continued to stir for additional 1hour to give a clear brownish red solution of $SeCl_2$ in THF.

Synthesis of telluropheno[2,3-c:5,4-c′]bipyridine(2c). To a stirred solution of 3,3′-dibromo-4,4′-bipyridine (628 mg, 2.0 mmol) in dry THF (60 mL) was added dropwise a solution of n-BuLi (2.5 M in hexanes, 1.68 mL, 4.2 mmol) via syringe at -94°C. After stirring for 1 hour at the same temperature, $TeCl_4$ (566 mg, 2.1 mmol) in THF (5 mL) was added dropwise to the above solution. The reaction mixture was then allowed to warm to the room temperature and stirring was continued overnight. After evaporation of the solvent under reduced pressure, the residue was taken up in CH_2Cl_2 (40 mL) and then added saturated Na_2S solution (20 mL). The reaction mixture was vigorous stirred at room temperature until the solution was clarified. The mixture was extracted several times with CH_2Cl_2 (40 mL each time), the combined organic phases were dried over anhydrous Na_2SO_4 and concentrated to give a brown oil, which was purified by column chromatography (SiO_2, petroleum ether/ethyl acetate, 1:1) to give 188 mg (33 %) of brown solid. ^{1}H-NMR (400 MHz, $CDCl_3$): δ/ppm=9.19 (s, 2H), 8.70 (d, 2H), 8.07 (d, 2H).

Synthesis of 4-(bromomethyl)-N-(4-(bromomethyl) phenyl)-N-phenylaniline (3). A mixture of 4,4′-(Phenylazanediyl)dibenzaldehyde (1.36g, 4.5mmol) and sodium borohydride (0.378 g, 10.0 mmol) in 120 mL of a mixed solvent of dry CH_2Cl_2 and ethanol (1:1) was stirred in the dark at room temperature overnight. 120 mL of water was then added to the above reaction mixture. The obtained mixture was extracted several times with $CHCl_3$ (120 mL each time), the combined organic phases were dried over anhydrous Na_2SO_4. After evaporation of the solvent under reduced pressure, the residual white powder was directly suspended in 50 mL of dry diethyl ether without further purification. Then a solution of phosphorus tribromide (514 μL, 5.4 mmol) in 10 mL of dry diethyl ether was added dropwise to the above suspension within 5 minutes at 0°C. The reaction mixture was allowed to warm to the room temperature, followed by overnight stirring in the dark. A mixture of ice water (60 mL) and saturated $NaHCO_3$ solution (30 mL) was added to the above reaction system. The reaction mixture was extracted several times with CH_2Cl_2 (60 mL each time), the combined organic phases were dried over anhydrous Na_2SO_4. After evaporation of the solvent under reduced pressure, a sticky light green solid (1.88 g, 96%) was obtained. ^{1}H NMR (400 MHz, CD_2Cl_2): δ/ppm= 7.31-7.26 (m, 6H), 7.11-7.09 (m, 3H), 7.03-7.01 (d, 4H), 4.52 (s, 4H). EI: calcd for $C_{20}H_{17}Br_2N$: 430.97; found: *m/z*=430.97 (M^+, 100%).

Synthesis of PCVTPA(5). A stirred mixture of 2 (1.0 mmol) and 3 (1.0 mmol) in DMF (30 m) was heated at 60°C for 5 days. The precipitate was isolated via vacuum filtration and washed with CH_2Cl_2 for several times (30 mL each time). The product was collected and dried under high vacuum at 65°C to give the polymer 4.

To 4 (0.5 mmol) dispersed in acetonitrile (30 mL) was added an excessive of methyl triflate at room temperature, followed by an overnight stirring. After reaction was finished, a 500 mL of ice methanol was added slowly to the above reaction system. The precipitate was isolated via vacuum filtration and washed with methanol for several times (50 mL each time). The product was collected and dried under high vacuum at 65°C to give the polymer 5.

5a PSVTPA: ^{1}H-NMR (400 MHz, CD_3CN): δ/ppm = 9.80 (s, 2H), 9.17-9.14 (m, 2H), 9.00-8.99 (m,2H), 7.52-7.07 (m, 13H, PhH), 5.95(s, 4H). ^{19}F NMR (400 MHz, CD_3CN): δ/ppm = -79.25 (s, CF_3); GPC: Mw =4.7×10^3, Mn=4.7×10^3 PD=1.00.

5b PSeVTPA: ^{1}H-NMR (400 MHz, CD_3CN): δ/ppm = 9.75 (s, 2H), 9.12-9.08 (m, 2H), 9.02-8.99 (m,2H), 7.52-7.10 (m, 13H, PhH), 5.91(s, 4H); ^{19}F NMR (400 MHz, CD_3CN): δ/ppm =-79.25 (s, CF_3): GPC: Mw=6.4×10^3, Mn=6.1×10^3, PD=1. 05.

5c PTeVTPA: ^{1}H-NMR (400 MHz, CD_3CN): δ/ppm = 9.69-9.65 (m, 2H), 8.97-8.92 (m,4H), 7.51-7.06 (m, 13H, PhH), 5.82(s, 4H); ^{19}F NMR (400 MHz, CD_3CN): δ/ppm = -79.17 (s, CF_3); GPC: Mw=5.9×10^3, Mn=4.9×10^3, PD=1.21.

Synthesis of PBPTPA. A stirred mixture of 4,4′-bipyridine (1.0 mmol) and 3 (1.0 mmol) in DMF (30 m) was heated at 60°C for 5 days. The precipitate was isolated via vacuum filtration and washed with CH_2Cl_2 for several times (30 mL each time). The product was collected and dried under high vacuum at 65°C to give the polymer 6.

To 6 (0.5 mmol) dispersed in acetonitrile (30 mL) was added an excessive of methyl triflate at room temperature, followed by an overnight stirring. After reaction was finished, a 500 mL of ice methanol was added slowly to the above reaction system. The precipitate was isolated via vacuum filtration and washed with methanol for several times (50 mL each time). The product was collected and dried under high vacuum at 65°C to give the polymer PBPTPA. ^{1}H-NMR (400 MHz, CD_3CN): δ/ppm= 9.01-8.98 (m, 4H), 8.45-8.43 (m, 4H), 7.45-7.07 (m, 13H, PhH), 5.79 (s, 4H); ^{19}F-NMR (400 MHz, CD_3CN): δ/ppm= -79.25 (s, CF_3); GPC: Mw=7.8×10^3, Mn=8.0×10^3, PD=1.10.

The synthetic routes of the monomers and polymers are shown in Figure S8.

Device fabrication and characterization

The ITO glass substrate was carefully precleaned sequentially with deionized water, acetone, and 2-propanol in an ultrasonic bath for 15 min, and then treated with oxygen plasma. A 100 μL of the sample solution (10 mg·mL^{-1}) in acetonitrile was spin-coated on the pre-cleaned ITO sheet at a spinning speed of 800 rpm for 20 s and then 1500 rpm for 45 s, followed by the removal of the solvent under vacuum at 60°C overnight.

Al top electrodes were deposited on the surface of active layer through a shadow mask at 10^{-7} Torr via E-beam evaporation. All electrical measurements were performed on a Keithley 4200 semiconductor parameter analyzer in ambient condition without any device encapsulation.

Structural modeling

All density functional theory (DFT) calculation was performed using the Gaussian 16 program. The B3LYP functional with D3 correction (Becke–Johnson damping) was used for geometry optimization in the ground state. The def2-SVP basis set was used. All geometry optimization was done in the gas phase. In order to simulate the UV/Vis spectra of the samples, TD-DFT calculations were carried out by using B3LYP functional and def2-SVP basis set. For better comparison to the experimental absorption spectra, the polarity of dichloromethane as solvent was added.

QUANTIFICATION AND STATISTICAL ANALYSIS

This study does not include statistical analysis or quantification.

ADDITIONAL RESOURCES

Additional resources containing the, NMR, XPS spectra, structural modeling UV-Vis spectra, ESP modeling images, cyclic voltammogram, can be found in the supplemental information.